Imaging of three-dimensional (Si,Ge) nanostructures by off-axis electron holography ☆

C.L. Zheng [a,1], K. Scheerschmidt [b,*], H. Kirmse [a], I. Häusler [a], W. Neumann [a]

[a] *Humboldt-Universität zu Berlin, Institut für Physik, D-12489 Berlin, Germany*
[b] *Max Planck Institut für Mikrostrukturphysik, Weinberg 2, D-06120 Halle, Germany*

ABSTRACT

Quantitative phase mapping in transmission electron microscopy is applied to image the three-dimensional (3D) morphology of (Si,Ge) islands grown on Si substrates. The phase shift of the transmitted electrons induced by the crystal inner potential was recorded by using off-axis electron holography. The analysis of the experimental data requires the knowledge of the mean inner potential (MIP) of the (Si,Ge) solid solution. The MIP was calculated using different models of isolated or bonded atoms, which are based on the interpolation of first principle data. The results are compared with structure modeling and related MIP calculations applying classical molecular dynamics (MD) simulations. For MD simulations bond order potentials were applied, which can take into consideration both electronic effects and elastic relaxations. The calculated mean inner potential is used to transform the phase shifts into thickness mapping for the reconstruction of the 3D island morphology. Both, phase shift due to dynamical electron diffraction and structural relaxation influence the resulting 3D reconstruction.

© 2012 Elsevier B.V. All rights reserved.

1. Introduction

Transmission electron microscopy (TEM) provides powerful tools to investigate nanostructures in solids. The composition, shape and strain state of nanostructures can be locally evaluated at an atomic level of resolution by means of TEM techniques. The reduced dimension of nanostructures has a strong influence on the confinement of electrons and determines the physical properties (see, e.g., [1] for a recent overview with respect to this topic). Conventional electron microscopy, however, can only record the amplitude (intensity) of the electron wave at the exit face of a sample, while a lot of useful information is missed, which is stored in the unrecorded phase of electrons. Electron holography, however, provides both the information from the amplitude and phase of the exit electron wave [2,3]. This enables to get additional information, and in the case of studying nanostructures, the influences of shape and strain to the scattered electrons can be separated.

The phase shift of electron waves transmitting samples will be modified by the crystal inner potential. By electron optical arguments, e.g. the phase grating approximation or the Wentzel–Kramers–Brillouin (WKB) method to solve the wave equation, the phase shift $\Delta\phi(x,y)$ of a transmitted electron wave at the exit plane (x,y) of a crystal with respect to those of the vacuum is proportional to a certain projection of the Coulomb potential [4–7]. For medium-resolution electron holography, according to the above mentioned approximations, the phase shift $\Delta\phi$ at the exit plane can be written as:

$$\Delta\phi(x,y) = C_E V_0 t(x,y) \tag{1}$$

Here, C_E is the interaction constant between fast electrons and matter (e.g., $C_E = 0.00729\ \mathrm{V^{-1}\,nm^{-1}}$ at 200 kV), V_0 is the mean inner potential (MIP in V), and $t(x,y)$ is the locally varying sample thickness.

Applying the simple relation for the phase shift Eq. (1), the MIP may be determined, e.g., from the gradient of the phase shift at wedge shaped samples [6,7]. On the other hand, if V_0 is known, the 2D map $\Delta\phi(x, y)$ of the shift of the wave phase can be transformed into a thickness map $t(x, y)$ for surface morphology reconstruction.

However, one should be aware of the following problems: The mean inner potential V_0 is not well defined, as already discussed by Max von Laue [8], which nowadays is considered in different context as, e.g., failure of Bethe approximation or vanishing V_0 for infinite crystals only [9–11]. One has to keep in mind that the

phase shift is not only proportional to the mean inner potential, it is also modified by defects, strain, composition changes, shape, and surface structure. The structural details influence the scattering behavior and create an exit wave, reflecting, in principle, all structural properties, which may be described sufficiently only using the full dynamical scattering theory. This means, the simple phase grating approximation of Eq. (1) is only valid if no diffraction contrast occurs and no magnetic fields exist. They has to be replaced by a solution of the Schrödinger equation of a realistic structure model or even at higher level, e.g., modeling structure and MIP using the Hartree–Fock approximation or the density functional theory (DFT) and including inelastic and multiple scattering effects etc. [11–18]. That is why the model of scattering itself also influences V_o. The often used simple model of non-binding approximation, also denoted as model of isolated atoms (see e.g. [3]), has to be replaced by evaluating the charge density. However, as will be shown, valuable MIP can be developed using suitable interaction potentials and classical molecular dynamics (MD) as, e.g., in [19], where the bond order potential is extended to fourth order approximation to include suitable σ- and π-bond interactions [20], which has the advantage to mimic the electronic terms and generate suitable structural models [21].

This paper illustrates the possibilities and limitations of the analysis of shape and morphology of (Si,Ge) islands by means of off-axis electron holography. The experimental details of crystal growth of (Si,Ge) islands, TEM investigations and off-axis electron holography are described in Section 2. The results of TEM and STEM investigations for the shape analysis are discussed in Section 3.1. The interpretation of the off-axis electron holography data using the phase grating approximation according to Eq. (1) provides the shape of the islands to a reasonable approximation (Section 3.2). Improvements of shape analysis using DFT and MD for simulation of the MIP of relaxed island structures are discussed critically in Section 4. Further possibilities for structure refinement of the described shape analysis, i.e., consideration of dynamical scattering effects and the influence of strain to MIP are outlined in Section 5.

2. Experimental details

Free standing (Si,Ge) islands were grown on (001) oriented Silicon substrates by liquid phase epitaxy (LPE) using Bismuth as solvent. The islands were grown at 600 °C close to the thermo-dynamical equilibrium, i.e., with a very low growth driving force. A detailed description of the growth process was given in [22]. Two samples with different dissolved Germanium mass (A: 0.207 g and B: 0.25 g) and different cooling rate (from 600° to 590°, A: 0.25 K/min and B: 0.5 K/min) were prepared and investigated in this work.

Plan-view samples were prepared for TEM investigations as follows. In order to preserve the original morphology and structure of the (Si,Ge) islands, the thinning procedures were always carried out from the back side of the Si substrate. First, the samples were mechanically pre-thinned to a thickness of about 80 μm, followed by cutting discs (diameter ∼3 mm) out of the wafer and dimpling to approximately 30 μm thicknesses. Finally, the ion milling (Ar$^+$) thinning with milling angle 5–10° was carried out until the thickness was down to transparency of the samples for electrons.

TEM investigations were performed on a JEOL JEM-2200FS field emission transmission electron microscope operated at an accelerating voltage of 200 kV. A Gatan 794 slow-scan charge-coupled device (CCD) camera (1024 × 1024 pixels) was used for digital recording. In addition, a JEOL high angle annular dark field detector was applied to acquire the STEM-HAADF images.

For off-axis electron holographic experiments, a thin platinum wire of 0.6 μm diameter and of 5 mm length was used as electrostatic biprism. The biprism was mounted in an individual retractable holder close to the first image plane, and can be moved in two horizontal directions (x: ± 1.5 mm, y: ± 1.0 mm) plus an 180° in-plane rotation. Under such construction, the biprism will be easily aligned parallel to the interface between the vacuum (reference wave) and the specific region of the sample (object wave).

In order to get large area phase mappings the electron holograms were recorded in Lorentz mode, which means the normal objective lens was switched off and the focusing function was replaced by an objective mini lens below the lower pole piece of the normal objective lens. The applied biprism voltage was set in the range of 70–80 V leading to an overlapping width of interference fringes from 2.5 μm to 3 μm. Therefore, a large area phase mapping up to half of the overlapping region can be achieved.

The amplitude and phase information of the electron exit wave were extracted from the recorded electron holograms by using digital Fourier transform and side band filtering [23]. During the phase reconstruction, reference holograms imaged in the vacuum region were applied to compensate the geometric distortions caused by the imaging and recording system. Further image processing was performed by the Gwyddion package [24]. The contributions of the wedged Si substrate to the total phase $\Delta\phi(x,y)$ shift was calculated with a polynomial fit of the phase image and subsequently removed as background. Then, following Eq. (1), the sample thickness $t(x,y)$ is given by

$$t(x,y) = \frac{\Delta\phi(x,y)}{C_E V_0}, \tag{2}$$

if the mean inner potential V_o of the crystal is known. Applying Eq. (2), the 2D map of the exit wave phase shift can be transformed into a thickness map (cf. Sections 3.2 and 3.3). Besides the holographic phase mapping (cf. Section 3.1 and Fig. 1), the morphology and the structure of the (Si,Ge) islands were also examined by conventional TEM (CTEM), electron diffraction and high-angle annular dark field scanning transmission electron microscopy (HAADF-STEM).

## 3. Results of TEM and off-axis electron holography

3.1. CTEM and HAAD-STEM studies of morphology and structure

Fig. 1a shows a plan-view [001] zone-axis bright field image of typical (Si,Ge) nanostructures (Sample A). Arrays of (Si,Ge) islands deposited on the Si substrate are clearly visible. The projection of the islands shows a quadratic base shape with a narrow size distribution. The average base width was determined to about 130 nm. Each of the islands exhibits a complex diffraction contrast due to thickness variation across the island. The inserted electron diffraction pattern in Fig. 1a clearly reveals that the (Si,Ge) islands have a good epitaxial orientation with the Si substrate, since only one set of diffraction spots is visible. Comparing the electron diffraction pattern with the bright field (BF) image, the four basal edges are determined to be parallel to the ⟨110⟩ directions of the Si substrate, while the vertical growth direction of the islands is determined along the [001] direction.

In the HAADF-STEM image of Fig. 1b, the (Si,Ge) islands show brighter contrast versus the substrate due to the larger thickness contributing to the scattering process. The Fourier transformed spectrum of the STEM image (inserted in the lower left of Fig. 1b) contains several discrete spots, revealing that the islands are
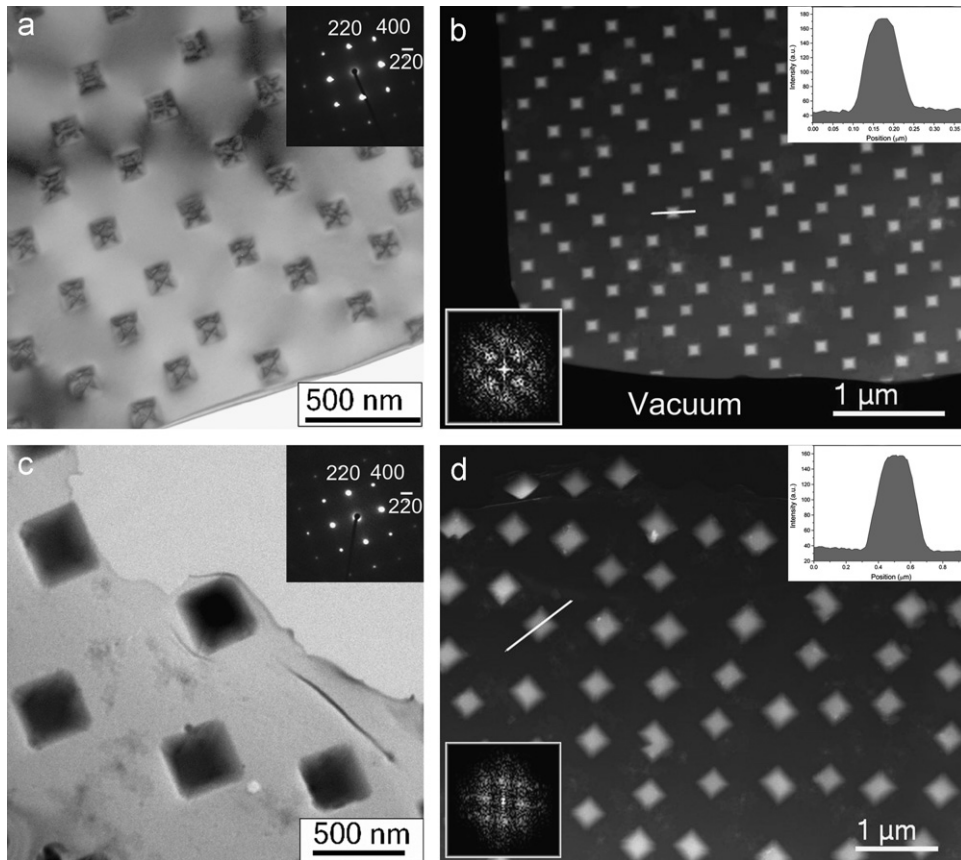
Fig. 1. (Si,Ge) islands grown on a (001) oriented Si substrate: (a) and (c) BF-TEM images in [001] zone axis orientation of sample *A* and *B*, respectively. Inserted are the corresponding SAED patterns. (b) and (d) HAADF-STEM images of sample *A* and *B*, respectively. The Fourier transformed spectrum, i.e. the optical diffraction of the STEM images, is inserted in the bottom left of each image. Intensity line profiles across an individual (Si,Ge) island as indicated in the images are inserted in the top right.
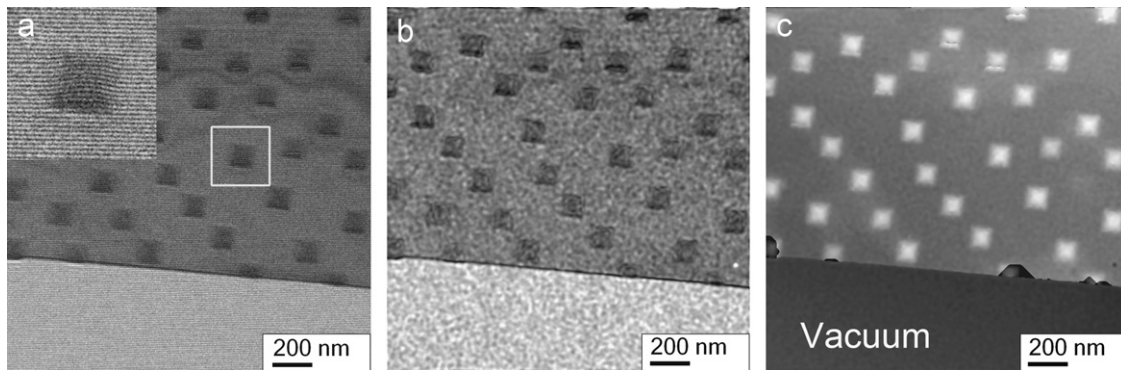
Fig. 2. (a) Electron hologram of (Si,Ge) islands on a (001) Si substrate (sample *A*). Insert: an individual enlarged island, (b) reconstructed amplitude image and (c) unwrapped phase image.

arranged almost like a two-dimensional lattice consisting of them. Such self-organized ordered structure indicates that the island growth occurs via the coherent strain-free Stranski-Krastanow growth mode [25]. During the early growth stages, surface ripples are developed due to the elastic stress relaxation. The ripples have a defined wavelength and form a two-dimensional pattern aligned along the in-plane $\langle 100 \rangle$ directions. Subsequently the ripples transform into pseudomorphic islands during the further growth process. The islands proceed to grow in vertical direction with fixed island width to form an ordered island structure, which has been proved by the BF- and STEM images. An individual island and the corresponding HAADF-STEM cross-section intensity profile along [110] direction is inserted at

the upper right of Fig. 1b. The intensity increases linearly from the edge to the center region and ends with a relative flat top. This indicates that the islands might have a truncated pyramidal shape. However, we do not get any quantitative thickness information from the BF- and HAADF-STEM images. The [001] zone-axis BF-TEM and the HAADF-STEM image of sample *B* are shown in Fig. 1c and d, respectively. The (Si,Ge) islands show a similar morphology like those in sample *A*, except the average basal width now is increased to about 350 nm.

It has been found that the basal width ω in such (Si,Ge) LPE-grown islands is limited solely by the misfit energy and scales therefore only with the Ge concentration x, that means, it does not depend on the growth velocity and the growth

temperature [25]. Thus, the concentration of Germanium x in $Si_{1-x}Ge_x$ islands can be evaluated from the empirical relationship $\omega \approx 18.62 \times x^{-2.01}$ of [26]. For sample A with the average basal width $\omega = 130$ nm, the concentration of Germanium is evaluated to about $x \approx 0.38$. For sample B, which has a larger average basal width $\omega = 350$ nm, the concentration of Germanium drops down to $x \approx 0.23$.

3.2. Electron holographic phase mapping

In order to get a quantitative thickness mapping of the (Si,Ge) nanostructures, 2D maps of electron phase shifts were recorded by electron holography as described in Section 2. Fig. 2a, b and c show the electron hologram, the reconstructed amplitude, and the unwrapped phase images of sample A, respectively. The electron hologram was imaged under weak diffraction conditions by tilting the sample several degrees away from [001] zone axis. From the electron hologram in Fig. 2a it can be seen that several tens of the islands are covered by the fine biprism fringes, the vacuum area at the bottom of the image was used for the transmission of the reference wave. A selected region of the hologram (outlined by the white frame) was magnified and inserted at the upper left of Fig. 2a. The brightness of the inserted image has been slightly adjusted for a better visualization of the fringes. From the enlarged hologram it can be clearly seen that the fringes are strongly distorted across the island, which indicates the large phase shift of the electrons due to the thickness variation across the island. The reconstructed amplitude image Fig. 2b is comparable with Fig. 1a, it looks like a conventional BF-TEM image with less of the special features, but more noisy. The corresponding unwrapped phase image is presented in Fig. 2c. The bright contrast of the (Si,Ge) islands again reveals the large phase difference between the islands and the substrate due to the different thickness.

For a better visualization of the phase shift within the (Si,Ge) islands, a part of the phase image Fig. 2c were further amplified and displayed in Fig. 3a. The phase spacing between the two neighbored black or white lines is approximately 0.2π. Each of the islands contains a set of high density square-shaped contour lines which is simultaneously scaled from the edge to the center region. Close to the center, the density of the contour lines decreases. A line profile of unwrapped phase across a single island is plotted in Fig. 3b. Considering the linear relationship between the phase shift and the sample thickness (Eq. 1), both Fig. 3a and b clearly indicates that the height of the islands linearly increases from the edges and ends with a relative flat top. This is consistent with the HAADF-STEM results. However, the phase shift of electrons here provides more quantitative data

about the height of the islands. Compared with the (Si,Ge) islands, the contiguous Si substrate in Fig. 3a exhibits a non-ordered pattern and indicates a relative small variation of local thickness by means of the bright to dark background change diagonally from lower left to upper right corner. Only at a much larger scale of about 200 nm and enlarging the phase scale, a phase shift of about 0.2π is visible, which is due to the wedge-shaped substrate. Both, the wedge-shaped sample and the tilt of the object to get the special imaging conditions as discussed in detail later interpreting the results, influence the holographic phases. As pointed out by Lehmann [27] the phase shifts due to wedge and tilt may be corrected by back-propagating the phase, however, the effects are relevant only for high-resolution imaging conditions. Here, the resulting phase shifts are less than a few percent of the shape and strain effects as can be seen comparing the phases on different positions outside the islands. The strain of the islands in the BF of Fig. 1a influences the thickness-bend contour locally, whereas only small contrast changes in greater areas demonstrate the flat phases. Thus all effects are corrected by background interpolation in the present work.
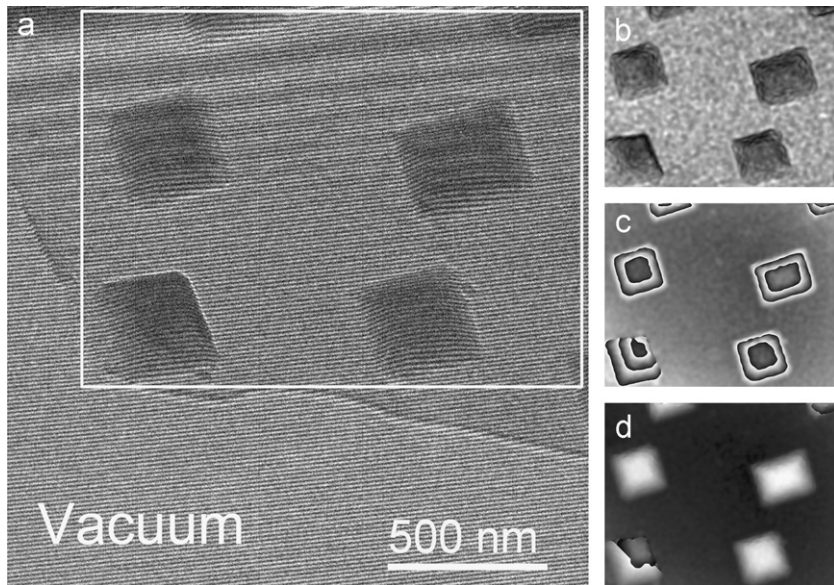
The electron hologram, the reconstructed amplitude, the raw phase as well as the unwrapped phase images of four islands of sample B are presented in Fig. 4a-d, respectively. Several contour lines with a phase spacing of 2π can be directly seen in the raw phase image, as shown in Fig. 4c and indicates a huge phase shift. The line profiles extracted from the corresponding amplitude and phase image of an individual island from Fig. 4 are compared in Fig. 5. An indication for the cross-section of the island parallel to the growth direction could be recognized from the phase profile. Contrary to that, the amplitude looks noisy and drops much faster very close to the edge. It does not show the shape, but an indication of the lattice deformations as will be discussed later in Section 4.

4. Discussion: interpretation of the phase maps by calculating the mean inner crystal potential

To avoid the problems in the definition of the mean inner crystal potential (MIP) as mentioned in the introduction, the analysis should be restricted solely to finite crystals as used in TEM. The MIP can then be defined as the volume average of the Coulomb potential of the crystal. When neglecting the surface effect, the MIP equals to the mean potential within a unit cell. However, ignoring surface effects yield to ambiguities mentioned with infinite periodic structures and do not give a relation between atomic form factors, electron densities, and the scattering potential [8–12].
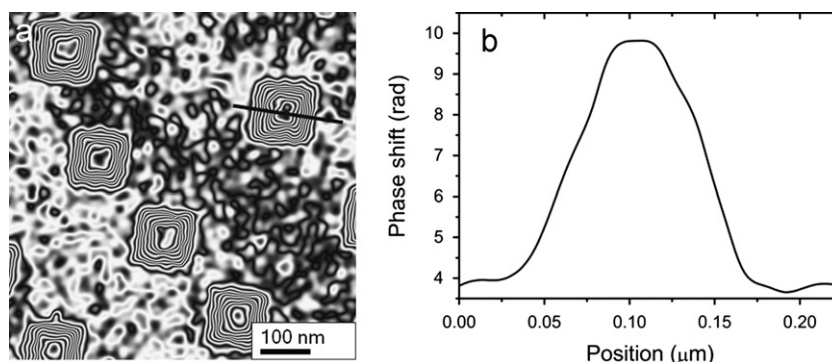
Fig. 3. Amplified phase image of (Si,Ge) islands on (001) oriented Si substrate (sample A). The corresponding black–white phase spacing is 0.2 π by enlargement, thus the crystal wedge is indicated by the diagonal bright and dark background contrast corresponding to 0.2π phase shift. (b) Unwrapped phase profile across the individual (Si,Ge) island as indicated in (a).

Fig. 4. Holographic electron wave reconstruction of (Si,Ge) islands grown on (001) orientated Si substrate (sample *B*): (a) electron hologram, (b) reconstructed amplitude, (c) raw phase (phase spacing: 2π) and (d) unwrapped phase image.
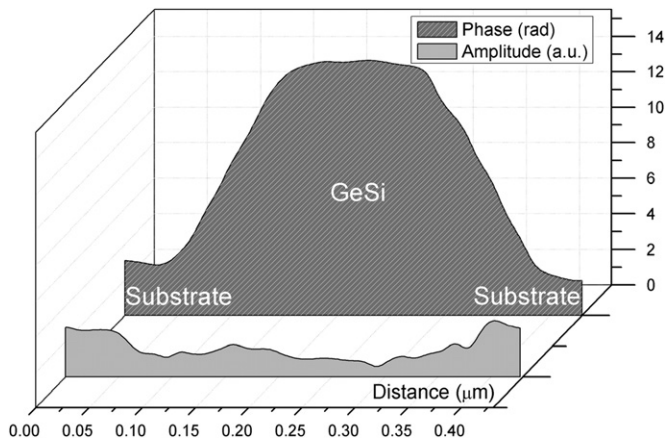
Fig. 5. Amplitude and phase profile across an individual (Si,Ge) island of sample *B*.

The simplest consideration is the model of isolated atoms [3] which is equivalent to the assumption that the optical potential of a crystal may be approximated by a sum of the contributions of the individual atoms. This means, the bonding between the atoms in a real crystal, charge exchange, and electron interaction effects are neglected. So the crystal potential can be considered as a superposition of the individual atomic potentials. The atomic potential for most of the elements has been calculated with ab initio computations, e.g., in [6,10–18]. In the applications of TEM, the atomic potential is normally expressed in the form of electron atomic form factors which are equivalent to the Fourier coefficients in an infinite periodic crystal [9,11–14]:

$$f(k) \sim V_k = -\frac{1}{\Omega} \int V(r) e^{-2\pi i k \bullet r} d^3 r \tag{3}$$

This is based on the fact that in the first Born approximation the scattering wave is proportional to the scattering potential, Ω is the volume of a unit cell, $\boldsymbol{k}$ can be replaced by the scattering vector. The average $V_0 = -1/\Omega \int V(r) d^3 r$ gives the MIP yielding:

$$V_0 = -\frac{2\pi \hbar^2}{me\Omega} \sum_j F(0) = -\frac{2\pi \hbar^2}{me\Omega} \sum_j f_j(0) \tag{4}$$

in the isolated atom model, with e the electron charge, m the electron mass, $\hbar$ the reduced Planck constant (giving the MIP in the unit of Volt V instead of eV), $F(0)$ the structure factor in forward direction, and $f_j(0)$ the corresponding atomic form factors of the j-th atom. (Si,Ge) crystallizes in the diamond structure with space group $Fd\overline{3}m$ having 8 atoms in the unit cell. Thus the structure factor of $Si_{1-x}Ge_x$ as a function of the Ge concentration x reads $\sum_j f_j(0) = 8 \times \{f_{Si}(0)(1-x)+f_{Ge}(0)x\}$. With the electron atomic form factor from Doyle and Turner [13] using relativistic Hartree–Fock atomic wave functions one gets $f_{Si}(0)=5.828$ Å and $f_{Ge}(0)=7.378$ Å. Including corrections for the lattice constant of the (Si,Ge) alloy the unit cell volume $\Omega=a^3$ yield to a slight non-linear fit. Together with V_o resulting from different other models, the resulting MIP of $Si_{1-x}Ge_x$ for this approximation is plotted in Fig. 6 as "SCFfit". As discussed in the following, all the MIP shown in Fig. 6 for comparison with the "SCFfit", are calculated for interpolated electron densities or applying MD simulations with the BOP and including structure relaxations.

Compared with neutral isolated atoms, the electron density and electrostatic potential distribution of atoms in a real crystal will be changed due to the bonding between atoms. The changes are greater in the shell part of the atoms and less in the core region. As first pointed out by Bethe, the MIP is sensitive to such redistributions of electrons, cf. [8–12,18]. In order to get accurate MIP-values, the electrostatic potential distributions in the crystal should be recalculated, which generally can be performed by calculating the electronic structure of crystals with first principle methods, e.g., using the density functional theory (DFT). The calculated ground state electron density $\rho(r)$ can be transformed into electro static potential distributions via Poisson equation. In terms of the electron density the MIP reads:

$$V_0 = -\frac{1}{\Omega_{crystal}} \iint \frac{\rho(r)}{|r-r'|} d^3 r' d^3 r \tag{5}$$

However, a higher effort in evaluating the full electron density $\rho(r)$ at the first principle level is necessary and the already mentioned surface charge problem of finite crystals needs reasonable atomic models or approximations, cf., e.g., [6,10–12,16].
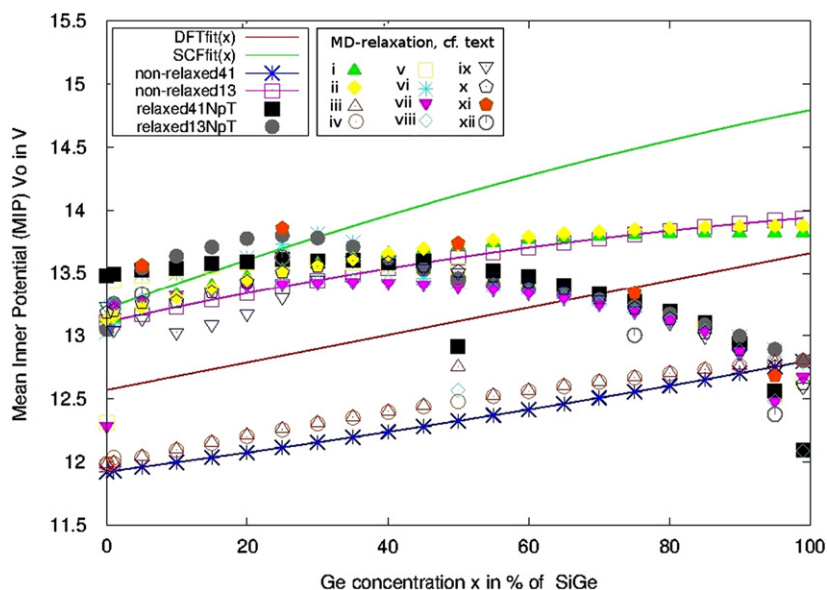
Fig. 6. Calculated mean inner potential (MIP: V_o in V) of $Si_{1-x}Ge_x$ as function of the Ge concentration x for different scattering models: "SCFfit"=isolated atom approximation; "DFTfit"=linear fitted DFT data; "non-relaxed/relaxed/13/41"=scan of the total energies from MD simulations with BOP and small-$(13 \times 13 \times 13)$ or large-$(41 \times 41 \times 41)$ vacuum super cells. The relaxed structures are simulated by annealing up to 400 K and assuming different conditions denoted with "i–xii", for details see text.

The higher effort results from both the shell and the core contributions of the atoms in a full electron calculation. Furthermore, the MIP of a crystal has to be referred to a reference zero potential point infinite away from the crystal. In order to get such a zero potential point, a large super cell containing both a few crystal layers and a vacuum layer should be included during the calculation. Obviously, when the structure itself already needs a large super cell as for an alloy, the calculation becomes very complex. A simple method may be to reduce the effort: the MIP of $Si_{1-x}Ge_x$ is estimated by a linear fitting of the MIP of perfect crystals which are calculated at the DFT level. Using the data of Kruse and Schowalter [6] one gets for Si 12.57 V and for Ge 14.67 V. Compared with the isolated atom model, the fitted value should be more realistic, since bonding effects are considered partially. The fitted data are plotted in Fig. 6 as "DFTfit". Compared to the data calculated with the isolated atom model denoted as "SCFfit", the fitted data are about 6%–9.8% smaller over the full range of Ge content. The MIP for sample A with a Ge concentration $x=0.23$ and B with $x=0.38$ results in $V_o=13.05$ V and $V_o=13.37$ V, respectively. These values are used both for the interpretation of the experimental results and as reference data in comparison to the other MIP-models.
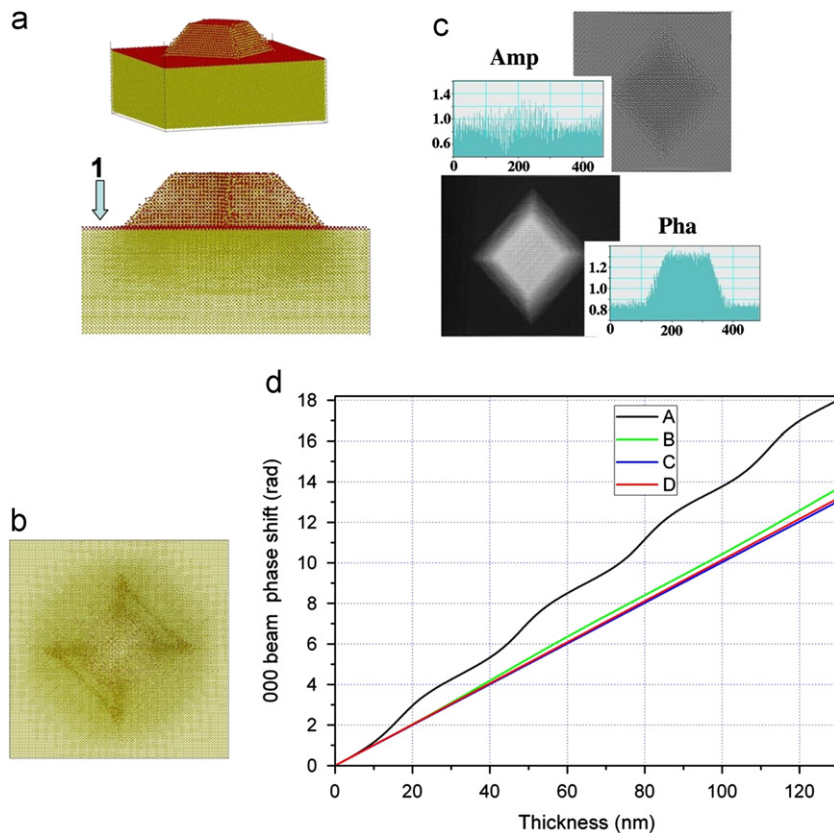
Molecular dynamics (MD) using a bond order potential (BOP, cf. [19–21] and references therein for development and application of a 4-th order approximation) provides a possibility to model both, the relaxation of nanostructures (with subsequent simulation of the exit wave phase, see below), and an alternative way to the evaluation of V_o by scanning the BOP itself. The latter is possible due the analytic approximation of a tight-binding potential, resulting in a force field like bond order potential. Here, a lot of different angular terms are included, which mimic the σ- and π- electronic bonds in addition to a repulsive part and a promotion term of the potential. In Fig. 6 different results to calculate V_o as function of the Ge concentration are shown to compare BOP based MD with the above discussed "SCFfit" and "DFTfit". The BOP data are extracted by scanning half filled super cells (SC) of (Si,Ge) with different Ge concentrations [21] created from $13 \times 13 \times 13$ or $41 \times 41 \times 41$ unit cells, which corresponds to 7 nm and 23 nm box lengths, respectively. The 7 nm SC

containing 10478 atoms will be denoted small SC (sSC), the 23 nm SC with 312666 atoms as extended (eSC). The Ge concentration x is varied randomly exchanging Si by Ge with the ratio x. The scans of the total energies include all attraction terms, i.e. σ-, π-bonds, promotion energy, and negative repulsive energy of the bond order potential for non-relaxed and relaxed structures, respectively.

The curves in Fig. 6 denoted by "non-relaxed13" and "non-relaxed41" are the result of scanning the total BOP energy for non-relaxed structures, i.e., only Si is randomly exchanged by Ge as described above for the sSC and eSC, respectively, and the atomic distances are those of Si. The other curves show calculated mean inner potentials of (Si,Ge) as function of the Ge concentration x after different MD-BOP structure relaxations. The static relaxation includes 30 steps gradient minimization of the structures and 2,000 steps of 0.5 fs MD run at 0 K. A full MD relaxation is like an annealing process using several 10,000 steps of 0.5 fs MD for a temperature regime from 0 K to 400 K and back to 0 K; all after a static pre-relaxation. During the relaxation either NpT or NVE control, i.e., constant pressure or constant volume conditions are applied. The MIP is determined again scanning the BOP total energy from the static relaxed structures, from snapshots at 400 K, which corresponds to one selected dynamics or from the final structure after the full annealing regime. The different conditions assumed for the MD structure relaxations and included in the Fig. 6 by the dots denoted with "i–xii", "relaxed13NpT", and "relaxed41NpT" are in detail as follows:

(1) Static relaxation: "i"=sSC, NVE, "ii"=sSC, NpT, "iii"=eSC, NpT, "iv"=eSC, NVE.
The static energy minimizations at 0 K show nearly the same behavior as the non-relaxed structures (cf. above). Both yield MIP similar to the SCFfit and the DFTfit, i.e., a nearly linear function of the Ge content. The shift of the curves is due to the remaining strain and the different normalization of the BOP bond energy. The slight curvature applying static minimization is due to the box lengths adaption different for NVE and NpT conditions, but similar to those discussed above for the "SCFfit".

Fig. 7. Molecular dynamics simulations with the bond order potential and calculated exit waves for a {110}-(Si,Ge)-pyramid, free-standing on (001)-Si with a mono-atomic Ge-wetting layer: (a) super cell of 23 nm box length in perspective and [100] view after relaxation via annealing at 400 K under NpT conditions. (b) [001] view showing the lattice deformations. (c) Multi-slice simulation of modulus and phase of the 200 keV exit wave of the relaxed model after tilting to [−1, 12, 120] zone axis, (d) multi-slice simulation of the dynamical phase of the cero beam in Si as function of the sample thickness: A=[001] zone axis. B=near [−1, 12, 120] zone axis. C=near [1,3,30] zone axis. D=Phase grating approximation, for details see text.

(2) Final structures (0 K–400 K–0 K) with full NpT-relaxation for sSC and eSC denoted "relaxed13NpT" and "relaxed41NpT", respectively, and related parameter variations:
"v"= eSC, NVE, "vi"= sSC, NVE, "xi"= sSC, NpT, weak p-control, "xii"= sSC, NpT, weak T-control.

(3) Selected dynamics at 400 K: "vii"=eSC, NVE, "viii"=eSC, NpT, "ix"=sSC, NVE, "x"=sSC, NpT.

The results for the relaxations at higher temperatures are illustrated by the dots in Fig. 6 which are not connected by lines. All dotted curves show nearly the same behavior, however, completely different than the curves discussed beforehand. The better relaxation for some hundred K yield to a non-linearity of the MIP as a function of the Ge concentration x which is, however, nearly independent from the special conditions as large or small SC, NpT or NVE, fully relaxed or at selected dynamics. The variety of the dots is related to the remaining residual strains in the relaxed structures due to the temperature or pressure rescaling conditions and the MD statistics. The average of the dots demonstrates the influence of strain and strain relaxation to the MIP.

Applying the MD with the bond order potential as mentioned above to a model of the free-standing (Si,Ge) island itself ({110}-pyramid on (001)-Si) enables the structural relaxation and a subsequent simulation of the exit wave function from the relaxed model. Fig. 7 shows one of the simulations, a relaxed pyramidal [110]-oriented island model in different views within a super cell of 23 nm to guarantee sufficient extension for MD-relaxation and subsequent multi-slice wave simulation. Fig. 7a gives a perspective view and the [100] orientation of the relaxed free standing uncapped island with 50% Ge in Si separated by a mono-atomic wetting layer from the Si

substrate. A detailed discussion of all simulations or even, if possible, an image matching, will be published elsewhere. The relaxation was performed using NpT conditions and annealing up and down from 0 K to 800 K in 100 K step with 1,000 cycles of 0.5 fs. Fig. 7b is a [001] view demonstrating the remaining strains or—after relaxation—better the lattice deformations due to the misfit at the interface. The model is divided in mono-atomic thin slices with the surface normal to [001] and the exit wave is calculated using multi-slice simulations [28]. Fig. 7c shows the result, the amplitude and phase of the scattered exit wave simulated with multi-slice at 200 keV incident beam energy for the model (a) after tilting the super cell to [−1, 12, 120] zone axis (as in experiment for special two beam incidence with high composition sensitivity). The phase profile clearly reveals the shape of the island with respect to the MIP and its extension as assumed in the model. The amplitude profile shows an oscillating behavior indicating the remaining strain as seen in Fig. 7b. Both, the amplitude and the phase may be compared with the experimental reconstructions of Figs. 2–4, the profiles especially with Fig. 5.

In addition, dynamical phase shifts of the transmitted beam as a function of the sample thickness for Si crystals were simulated with the multi-slice method (JEMS package [29]) using 200 keV incident beam energy, and atomic form factors according to the isolated atomic model, i.e., a MIP for Si of 13.91 V (cf. assumption "SCFfit" of Fig. 6). Fig. 7d shows the phase profiles for thicknesses up to 130 nm and different crystallographic orientations, denoted by A-D. The results for Si and (Si,Ge) are very similar and demonstrate the good linearity for the special image conditions chosen here. Curve A shows the simulated phase of the (000) beam in Si [001] zone axis
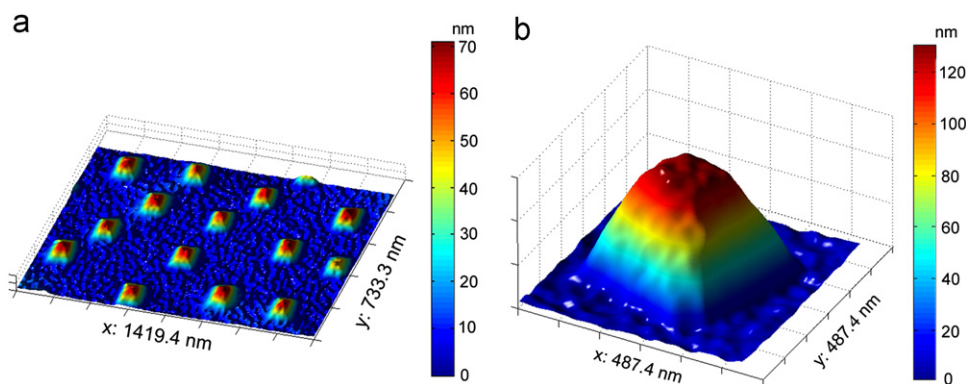
Fig. 8. Reconstructed 3D shape and morphology of (Si,Ge) islands grown on (001) oriented Si substrate according to the transformed phase maps using the DFT based MIP V_0: (a) sample A and (b) sample B.

orientation, the phase exhibits a slight oscillating behavior. This leads to a large phase difference compared with the phase shift according Eq.(1). Contrary to that, the simulated phases of the 000 beam in the weak diffraction conditions (B–D) are similar to the experiments for sample A and B and show a good linear relationship between phase and sample thickness (The parameter are in detail: (B) (-1.68, 22.14, 0) center of Laue zone, close to [-1, 12, 120] zone axis. (C) (6.39, 21.06, 0) center of Laue zone, close to [1,3,30] zone axis. (D) phase shift according to the phase grating approximation Eq. 1). This indicates that under weak dynamical diffraction conditions, the relationship between phase and thickness according to Eq. (1) can be well satisfied.

Finally, with the fitted data of MIP, and the knowledge of the lateral extension of the QD from the amplitude contrast, the 2D phase mapping is transformed into the 3D images of Fig. 8 by using of Eq. (3). The resulting 3D morphology of the (Si,Ge) islands of sample A is shown in Fig. 8a. The islands have a truncated pyramidal shape with heights between 60 nm and 70 nm. The 3D geometry of sample B is shown in Fig. 8b. The island again shows a truncated pyramidal shape. It can be seen that with the increasing lateral size of the islands to 350 nm, the island height is also increased to approximately 130 nm. It would be of great interest to clarify in future the details of the morphology, whether they are revealing really surface details, or diffusion and strain gradients according to the dependencies of MIP as demonstrated in Fig. 6. In addition, the question has to be solved, whether the MD-corrected MIP enables also phase corrections.

5. Conclusion

The electron holographic exit wave reconstruction enables the quantitative determination of shape and morphology of nanostructures and, in principle, to separate it from stoichiometry and strain, using the additional information given by the phase of the scattered wave. However, the phase grating approximation Eq. (1) is only valid for kinematical diffraction conditions. For thicker crystals, dynamical diffraction effects cannot be avoided. Though the samples investigated in this work have been tilted away from [001] zone axis into week diffraction conditions, the dynamical diffraction effects influence the phase of transmitted beam and thus the resulting thickness map according Eq. (2). To get a more quantitative analysis, in addition, a good model is necessary to simulate the mean inner potential. The comparison of the isolated atom model, DFT, and molecular dynamics simulations applying a bond order potential demonstrate the modification of the mean inner potential by the full electron density and lattice deformations. Therefore, the complete analysis of the morphology and structure of the islands has to be made by trial and error image matching including the full simulation of a structure model, the electron density and the dynamical scattering process. Furthermore, it should be proved how the influence of strain to the MIP can be included in forthcoming investigations.

References

[1] G.B. Biasiol, S. Heun, Compositional mapping of semiconductor quantum dots and rings, Physics Reports 500 (2011) 117–173.
[2] H. Lichte, P. Formanek, A. Lenk, M. Linck, C. Matzeck, M. Lehmann, P. Simon, Electron holography: Applications to materials questions, Annual Review of Materials Research 37 (2007) 539–588.
[3] E Völkl, L.F. Allard, D.C. Joy, Introduction to electron holography, Kluwer Academic, New York, 1999.
[4] M.R. McCartney, D.J. Smith, Electron holography: Phase imaging with nanometer resolution, Annual Review of Materials Research 37 (2007) 729–767.
[5] M. Gajdardziska-Josifovska, M.R. McCartney, W.J. deRuijter, D.J. Smith, J.K. Weiss, J.M. Zuo, Accurate measurements of mean inner potential of crystal wedges using digital electron holograms, Ultramicroscopy 50 (1993) 285–299.
[6] P. Kruse, M. Schowalter, D. Lamoen, A. Rosenauer, D. Gerthsen, Determination of the mean inner potential in III–V semiconductors, Si and Ge by density functional theory and electron holography, Ultramicroscopy 106 (2006) 105–113.
[7] D. Cooper, C. Ailliot, J.-P. Barnes, J.-M. Hartmann, P. Salles, G. Benassayag, R.E. Dunin-Borkowski, Dopant profiling of focused ion beam milled semiconductors using off-axis electron holography; reducing artifacts, extending detection limits and reducing the effects of gallium implantation, Ultramicroscopy 110 (2010) 383–389.
[8] M. von Laue, Materiewellen und ihre Interferenzen, 2. Aufl., Akademische Verlagsgesellschaft Geest & Portig, Leipzig, 1948.
[9] L.M. Peng, S.L. Dudarev, M.J. Whelan, High-energy electron diffraction and microscopy, Oxford University Press, Oxford, New York, 2004.
[10] P. Becker, P. Coppens, About the Coulomb potential in crystals, Acta Crystallographica Section A 46 (1990) 254–258.

[11] M. O'Keeffe, J.C.H. Spence, On the average Coulomb potential (Φ_0) and constraints on the electron-density in crystals, Acta crystallographica Section A 50 (1994) 33.

[12] M.Y. Kim, J.M. Zuo, J.C.H. Spence, LDA Ab-initio, calculations of the mean Coulomb potential V_0 in slabs of crystalline Si, Ge and MgO, Physica Status Solidi A: Applications and Materials Science 166 (1998) 445–451.

[13] P.A. Doyle, P.S. Turner, Relativistic Hartree–Fock X-ray and electron scattering factors, Acta crystallographica Section A 24 (1968) 390–398.

[14] H. Yoshioka, Effect of inelastic waves on electron diffraction, Journal of the Physical Society of Japan 12 (1957) 618–628.

[15] P. Rez, Virtual inelastic-scattering in high-energy electron-diffraction, Acta crystallographica Section A 34 (1978) 48–51.

[16] A.G. Fox, M.A. O'Keeffe, M.A. Tabbernor, Relativistic Hartree–Fock X-ray and electron atomic scattering factors at high angles, Acta Crystallographica Section A 45 (1989) 786–793.

[17] D. Rez, P. Rez, I. Grant, Dirac–Fock calculations of X-ray-scattering factors and contributions to the mean inner potential for electron-scattering, Acta Crystallographica Section A 50 (1994) 481–497.

[18] D.K. Saldin, J.C.H. Spence, On the mean inner potential in high-energy and low-energy electron diffraction, Ultramicroscopy 55 (1994) 397–406.

[19] V. Kuhlmann, K. Scheerschmidt, σ-bond expression for an analytic bond-order potential: including π- and on-site terms in the fourth moment, Physical Review B 76 (2007) 014306 (8 pages).

[20] K. Scheerschmidt, V. Kuhlmann, Relaxation of semiconductor nanostructures using molecular dynamics with analytic bond order potentials, International Journal of Materials Research 98 (2007) 1081–1085.

[21] K. Scheerschmidt, C.L. Zheng, H. Kirmse, I. Häusler, W. Neumann, Molecular dynamics simulations of (Si,Ge) quantum dots to quantify the shape analysis by electron holographic phase measurement, in: Proceedings of the 17th International Microscopy Congress ICM 17, Rio de Janeiro, 2010, p.18.4 (2 pages).

[22] M. Schmidbauer, T. Wiebach, H. Raidt, M. Hanke, R. Kohler, H. Wawra, Ordering of self-assembled $Si_{(1-x)}Ge_{(x)}$ islands studied by grazing incidence small-angle x-ray scattering and atomic force microscopy, Physical Review B 58 (1998) 10523–10531.

[23] M. Lehmann, H. Lichte, Tutorial on off-axis electron holography, Microscopy and Microanalysis 8 (2002) 447–466.

[24] D. Nečas, P. Klapetek, Gwyddion, ⟨http://gwyddion.net⟩, 2008.

[25] W. Dorsch, B. Steiner, M. Albrecht, H.P. Strunk, H. Wawra, G. Wagner, The transition from ripples to islands in strained heteroepitaxial growth under low driving forces, Journal of Crystal Growth 183 (1998) 305–310.

[26] W. Dorsch, H.P. Strunk, H. Wawra, G. Wagner, J. Groenen, R. Carles, Strain-induced island scaling during $Si_{1-x}Ge_x$ heteroepitaxy, Applied Physics Letters 72 (1998) 179–181.

[27] M. Lehmann, Exit surface dependence of the wavefunction measured and corrected by means of off-axis electron holography, Physica Status Solidi A: Applications and Materials Science 202 (2005) 2386–2396.

[28] P.A. Stadelmann, EMS-JEMS Java Version, ⟨http://cimewww.epfl.ch/people/stadelmann/jemsWebSite/jems.html⟩, 2004.

[29] M. Schowalter, K. Müller, A. Rosenauer, Scattering amplitudes and static atomic correction factors for the composition-sensitive 002 reflection in sphalerite ternary III–V and II–IV semiconductors, Acta Crystallographica Section A68 (2012) 68–76.